PAPER • OPEN ACCESS

Simultaneous mapping of cathodoluminescence spectra and backscatter diffraction patterns in a scanning electron microscope

To cite this article: Paul R Edwards *et al* 2024 *Nanotechnology* **35** 395704

View the article online for updates and enhancements.

Simultaneous mapping of cathodoluminescence spectra and backscatter diffraction patterns in a scanning electron microscope

Paul R Edwards[1,*] , **G Naresh Kumar**[1,2] , **Jonathan J D McKendry**[3] , **Enyuan Xie**[3] , **Erdan Gu**[3] , **Martin D Dawson**[3] and **Robert W Martin**[1]

[1] Department of Physics, SUPA, University of Strathclyde, 107 Rottenrow, Glasgow G4 0NG, United Kingdom
[2] School of Physics and Astronomy, Cardiff University, Maindy Road, Cardiff CF24 3AA, United Kingdom
[3] Institute of Photonics, Department of Physics, SUPA, University of Strathclyde, 99 George St., Glasgow G1 1RD, United Kingdom

E-mail: paul.edwards@strath.ac.uk

CrossMark

Abstract

Electron backscatter diffraction and cathodoluminescence are complementary scanning electron microscopy modes widely used in the characterisation of semiconductor films, respectively revealing the strain state of a crystalline material and the effect of this strain on the light emission from the sample. Conflicting beam, sample and detector geometries have meant it is not generally possible to acquire the two signals together during the same scan. Here, we present a method of achieving this simultaneous acquisition, by collecting the light emission through a transparent sample substrate. We apply this combination of techniques to investigate the strain field and resultant emission wavelength variation in a deep-ultraviolet micro-LED. For such compatible samples, this approach has the benefits of avoiding image alignment issues and minimising beam damage effects.

Keywords: cathodoluminescence, EBSD, hyperspectral, strain, ultraviolet, microLED, CL

1. Introduction

Cathodoluminescence (CL) hyperspectral imaging in a scanning electron microscope (SEM) can map subtle shifts in the emission wavelength of a semiconductor, on a sub-micron length scale. Many effects contribute to these spectral shifts, including variations in alloy composition, concentration of charge carriers, temperature, and elastic strain. The latter is well known to cause shifts in the emission through changes in the bandgap energy and/or due to the effects of induced piezoelectric fields. In thin-film semiconductors, such strain fields commonly originate at hetero-interfaces due to lattice or thermal mismatch, or around an extended crystal defect. Measuring, understanding and controlling this strain is an essential factor in optimising semiconductor devices.

This sensitivity of CL to strain fields has led to the technique being used as an indirect probe of the variation of strain

with position in a sample [1]. CL hyperspectral images are acquired, in which a spectrum is recorded at each spatial position in a scan. Least-squares fitting to each spectrum in the resultant data cube extracts peak positions which are then plotted as a map of wavelength or energy shift, from which the strain can be inferred. For example, this has previously been used to observe the relaxation of compressive strain through a blue-shift at the periphery of green-emitting $In_xGa_{1-x}N$/GaN microLED pillar structures [2].

More direct measurement of the crystal lattice can be carried out in an SEM using electron backscatter diffraction (EBSD). This technique is long-established in the mapping of crystal orientations in the grains of polycrystalline materials, and the value of correlating such information with CL maps of the same area has been demonstrated for both geological [3] and semiconductor thin-film [4] samples. In the last few years the EBSD technique has been extended to allow a full strain tensor to be extracted from small distortions in the diffraction pattern, using cross-correlation data analysis methods [5]. This development has been shown to be effective in revealing the strain fields associated with the dislocations which pervade nitride thin-films [6], and recent work compared the strain measured using this technique to that inferred through *ex-situ* CL and Raman mapping, finding good quantitative agreement [7].

While the two techniques are clearly complementary, *simultaneous* measurement of the strain (using EBSD) and its effect on emission (using CL) has not been previously demonstrated in a single scan, due to conflicting measurement geometries [7] and/or the need to use different instruments [4]. Both techniques would ideally have access to a large solid angle directly above the sample surface, and so each would obscure the other. However, if it were possible, such measurements would be advantageous in reducing beam damage and eliminating registration errors, by avoiding the need for multiple scans. Here we report on a method of achieving this goal for samples with a transparent substrate.

2. Method

The sample was fabricated from a commercial UV-LED wafer (*Qingdao Jason Electric Co. Ltd*) with a peak emission wavelength of 272–273 nm. This consisted (figure 1) of a double-polished *c*-plane sapphire substrate on which the following nitride layers were grown: AlN buffer (2 μm); *n*-type $Al_{0.6}Ga_{0.4}N$ (2 μm); six quantum wells of $Al_{0.45}Ga_{0.55}N$ (2.5 nm) with $Al_{0.55}Ga_{0.45}N$ (13 nm) barriers; $Al_{0.6}Ga_{0.4}N$ electron blocking layer (50 nm); and *p*-type GaN (310 nm). Pillars of 40 μm diameter were fabricated from the material using inductively coupled plasma etching. Metal contacts were applied to form fully functioning micro-LEDs, which were reported elsewhere [8]; however, the devices used here were left uncontacted to allow electron beam access and to allow backscattered electrons to exit for the EBSD. An SEM secondary electron image of the sample (of the same mesa, and acquired immediately before the EBSD/CL scan) is shown
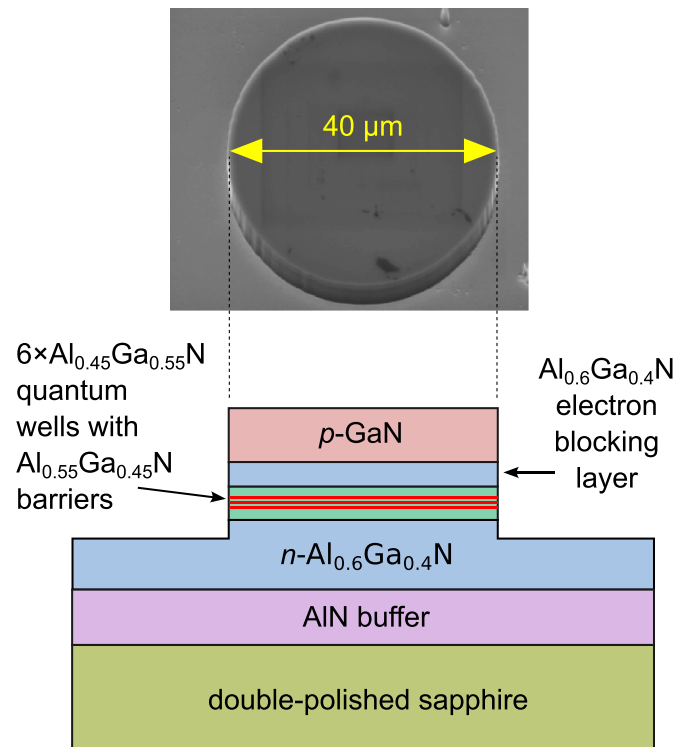
Figure 1. Structure of the AlGaN microLED sample, with tilt-corrected secondary electron image acquired at a 45° sample angle. Layer thicknesses are not to scale.
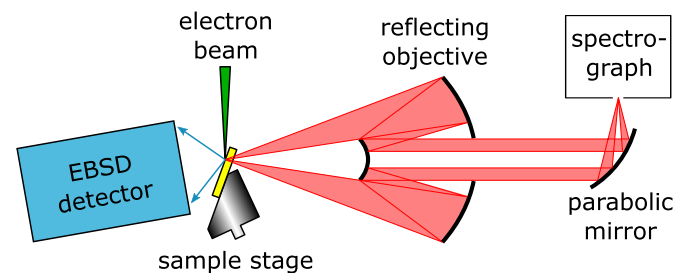
Figure 2. Setup used for simultaneous CL and EBSD.

above the schematic in figure 1; this image was acquired at a 70° sample angle and has been tilt-corrected.

The LED structure is designed for light emission through the transparent substrate, and the narrower-bandgap and strongly absorbing GaN *p*-layer would prevent measurement of luminescence through the top of the sample in the usual CL setup geometry [9]. We therefore measure the emitted light through the substrate, leaving exclusive access to the top surface for our EBSD detector. This setup is shown in figure 2.

The measurement is carried out in a field-emission SEM (*FEI Quanta 250FEG*) fitted with a commercial EBSD detector (*Oxford Instruments Nordlys*). The sample is inclined 70° towards this detector, while the CL is collected from the opposite side of the SEM by a reflecting objective focused through the double-polished sapphire substrate. This is a modified form of a customized CL setup described previously [10]. The light is focussed to the 50 μm entrance slit of a $\frac{1}{8}$ m

spectrograph (*Oriel MS125*), in which it is dispersed with a 1200 lines mm^{-1} grating and detected using a charge-coupled device (*Andor Technology Newton EMCCD*). This gives a spectral resolution of 2.0 nm, equivalent to 37 meV at 4.8 eV. A background spectrum was generated by acquiring 100 spectra with the electron beam blanked; these were averaged, and the result subtracted from each of the CL spectra acquired.

An electron beam energy of 30 keV is chosen to favor the EBSD measurement, higher than would usually be used for CL. The beam current is not directly quantified in this measurement, but is ≈1 nA. The scan is controlled by the external scan generator of the EBSD system, and a scan rate of 1 s/pixel ensures electron backscatter patterns (EBSPs) of sufficient quality for later processing. A raw EBSP is saved at each of the 149×130 pixels of the map, with a step size of 400 nm. The aspect ratio of the raster area is tilt-corrected in the microscope.

Synchronisation between the EBSD and CL acquisition is achieved by monitoring the staircase-shaped ramp signal of the fast (x) scan axis, which is high-pass filtered and further conditioned to provide the 5 V TTL pulse train required for the CCD hardware trigger. A full luminescence spectrum is thus recorded at each pixel during the EBSD mapping in order to simultaneously build up a CL hyperspectral image.

3. Results

3.1. CL

The acquired CL hyperspectral image was observed to be dominated by three peaks, each of which we fitted to a Gaussian function. A linear background was also included in the fit, taking into account the tail of a broad defect band evident at the low-energy end of the spectrum. Maps of the fit parameters of each Gaussian (intensity, centre energy and width) are shown in (figure 3).

Peak 1 (4.5–4.6 eV): Quantum well emission, matching the peak wavelength of 272–273 nm observed in the electroluminescence spectrum. This is consistent with the fact that the peak is emitted almost exclusively from the unetched mesa region. While there is significant inhomogeneity seen in both the peak energy and width maps, there is evidence of a red-shift in the emission at the edges of the mesa. Note that those pixels where the emission intensity approaches zero (mostly outside of the mesa) have been masked in black for clarity in the peak energy and FWHM maps, since these parameters are ill-defined in this case.

Peak 2 (4.7–4.8 eV): This peak is observed from both the etched and unetched areas, from which we infer that it originates from the 2 μm n-type Al$_{0.6}$Ga$_{0.4}$N layer. A narrowing and red-shifting of this peak is seen in the unetched mesa region compared with the surrounding etched material. This is indicative of increased self-absorption of light generated in the (thicker) mesa before it can emerge through the substrate; preferential absorption of the shorter wavelengths results in a narrower band of longer average wavelength light

being emitted. Despite this effect, and the significant homogeneity (hexagonal features related to Al/Ga ratio fluctuations in the wafer material), this peak also shows a clear red-shift at the edge of the mesa compared to its centre.

Peak 3 (5.0 eV): Because of its lower intensity, and to help avoid over-parametrising the fit, the centre energy and FWHM of this peak were kept fixed. The fitted intensity map shows that the peak is only emitted from the etched region, yielding little information on the microLED structure itself. The only nitride layer which could be excited selectively when the beam is in this region is the AlN buffer, from which broad defect emission bands may be expected. Light at this end of the spectrum will also be strongly absorbed as it passes through the rest of the buffer layer, and we may be observing what little light remains after this loss.

While spatial inhomogeneity is observed in all three emission peaks, no clear correlation is seen between this and any observable surface features in the corresponding SE image. The extent to which the observed peak shifts are due to elastic strain can now be investigated by comparing with the simultaneously-acquired EBSD.

3.2. EBSD

The recorded array of EBSPs was post-processed using commercial cross-correlation-based software (*CrossCourt4*). Referred to as high angular resolution EBSD (HR-EBSD), this analysis technique involves measuring the distortion of each pattern with respect to that at a user-chosen reference pixel to calculate maps of the full (relative) strain tensor [5]. This tensor ϵ is notated as

$$\epsilon = \begin{bmatrix} \epsilon_{xx} & \epsilon_{xy} & \epsilon_{xz} \\ \epsilon_{yx} & \epsilon_{yy} & \epsilon_{yz} \\ \epsilon_{zx} & \epsilon_{zy} & \epsilon_{zz} \end{bmatrix}, \tag{1}$$

where each tensor element ϵ_{ij} describes the variation of the displacement field $\boldsymbol{u}$ in the i and j axes:

$$\epsilon_{ij} = \frac{1}{2} \left(\frac{\partial u_i}{\partial u_j} + \frac{\partial u_j}{\partial u_i} \right). \tag{2}$$

The diagonal elements ϵ_{ii} are thus the normal (i.e. compressive/tensile) strains in the coordinate axes, while the off-diagonal elements (representing shear strain) are symmetric ($\epsilon_{ij} = \epsilon_{ji}$, as evident from equation (2)).

Figure 4 shows the results of the HR-EBSD analysis, where the redundant sub-diagonal elements of the symmetric tensor are omitted for clarity. A point near the map centre has been chosen as the reference position with respect to which the relative strain is determined. The results are displayed in a Cartesian coordinate system, where: $\boldsymbol{x}$ is the horizontal scan direction, which is also a direction within the sample plane; $\boldsymbol{y}$ is the direction normal to this in the sample plane (not the scan plane, given that the sample is tilted), and $\boldsymbol{z}$ is the sample normal direction, corresponding in this case to the c crystal axis of the wurtzite structure.
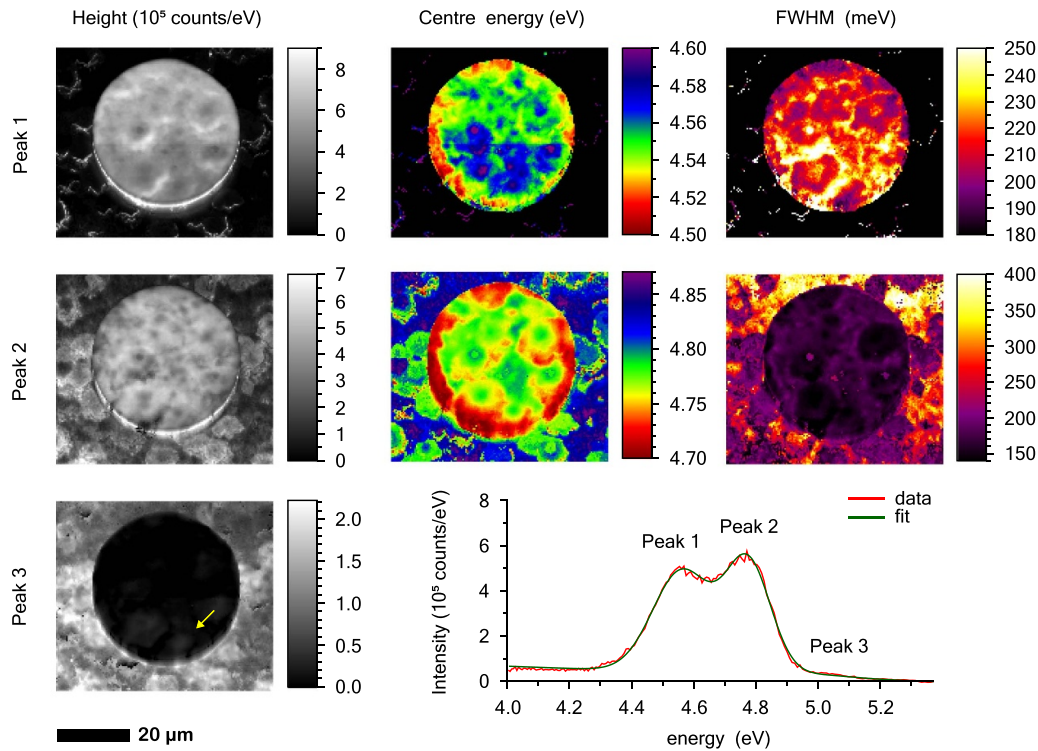
Figure 3. Results of fitting three Gaussian peaks to the CL hyperspectral image. Maps of the peak intensity, centre wavelength and FWHM are shown except for the lower intensity peak 3 whose spectral position was fixed at 5.0 eV to avoid over-parameterization. Pixels in which the peak intensity approaches zero are masked in black on the peak energy and FWHM maps. The example spectrum was extracted from the pixel marked with an arrow.
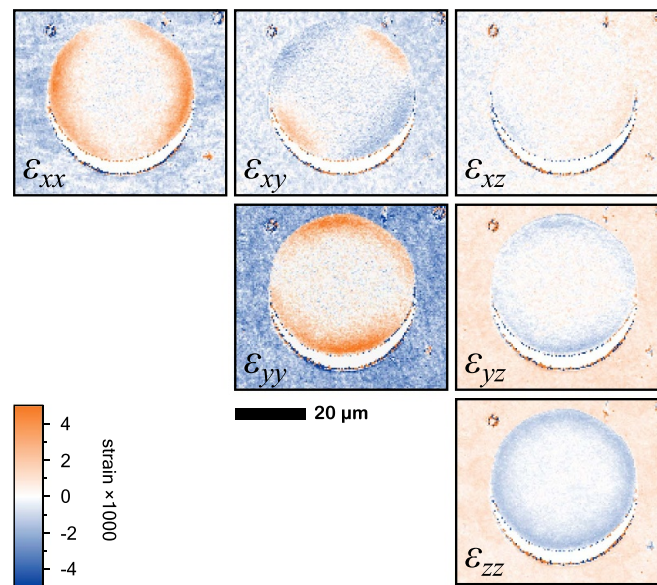
Figure 4. HR-EBSD results showing the strain tensor expressed in Cartesian coordinates. The map for each tensor element is shown on a common colour scale, representing $\epsilon_{ij} = \pm 0.5\%$. (Note that values are positive or negative for normal strain components which are relatively tensile or compressive, respectively.).

The greater magnitude of the 2×2 subset of strain components in the top left of the tensor (ϵ_{xx}, $\epsilon_{xy} = \epsilon_{yx}$ and ϵ_{yy}, together representing the in-plane strain) is an expected consequence of the free sample surface, since the out-of-plane stress will be zero. The out-of-plane normal strain component ϵ_{zz} appears to vary symmetrically, becoming relatively more compressive towards the mesa perimeter. However, this is less clearly visualised in the normal (ϵ_{xx}, ϵ_{yy}) and shear (ϵ_{xy}) components of the *in-plane* strain, where the apparent variation of the magnitude of the strain components around the device is an artefact of the different sample and tensor coordinate system geometries.
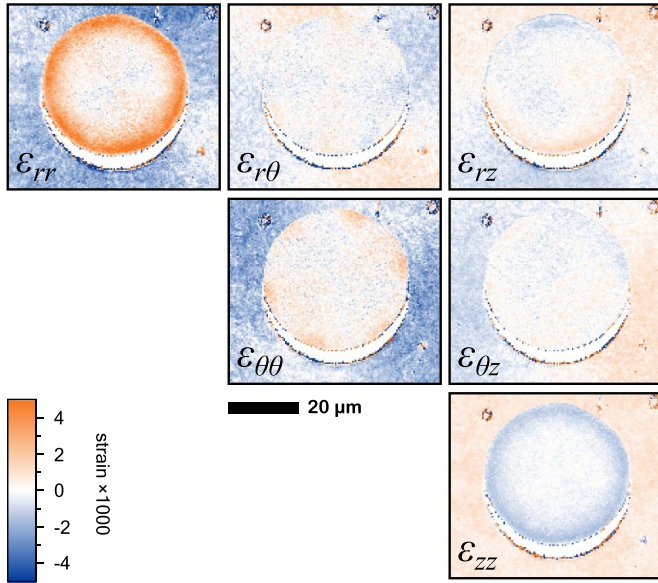
Figure 5. The same data as shown in figure 4, after transformation to a cylindrical polar coordinate system using equation (4). The strain magnitudes are again shown using the same colour scale.

One approach to resolving this visualization issue would be to map the *principal* strain: i.e. calculate for each pixel the unique direction for which the non-diagonal tensor elements equal zero, and the corresponding magnitude of the normal strain in this direction. In our case, though, we are helped by prior knowledge of the symmetry of this simple cylindrical structure. We therefore opt to display the strain using cylindrical polar coordinates (r, θ, z) whose axes are defined by the position of the centre of the microLED (which we estimate) and the direction of the sample normal (which remains the z axis). This is simply achieved using the orthogonal transformation matrix $\boldsymbol{Q}$ and its transpose $\boldsymbol{Q}^T$

$$\boldsymbol{Q} = \begin{bmatrix} \cos\theta & \sin\theta & 0 \\ -\sin\theta & \cos\theta & 0 \\ 0 & 0 & 1 \end{bmatrix}, \boldsymbol{Q}^T = \begin{bmatrix} \cos\theta & -\sin\theta & 0 \\ \sin\theta & \cos\theta & 0 \\ 0 & 0 & 1 \end{bmatrix} \quad (3)$$

to convert between the two coordinate systems [11], using:

$$\begin{bmatrix} \epsilon_{rr} & \epsilon_{r\theta} & \epsilon_{rz} \\ \epsilon_{\theta r} & \epsilon_{\theta\theta} & \epsilon_{\theta z} \\ \epsilon_{zr} & \epsilon_{z\theta} & \epsilon_{zz} \end{bmatrix} = \boldsymbol{Q} \times \begin{bmatrix} \epsilon_{xx} & \epsilon_{xy} & \epsilon_{xz} \\ \epsilon_{yx} & \epsilon_{yy} & \epsilon_{yz} \\ \epsilon_{zx} & \epsilon_{zy} & \epsilon_{zz} \end{bmatrix} \times \boldsymbol{Q}^T. \quad (4)$$

Tensor component maps in the new coordinate basis are thereby calculated from the old ones, for example:

$$\epsilon_{rr} = \left(\cos^2\theta\right)\epsilon_{xx} + \left(2\cos\theta\sin\theta\right)\epsilon_{xy} + \left(\sin^2\theta\right)\epsilon_{yy} \quad (5)$$

and so on. Figure 5 shows the HR-EBSD results after this transformation into cylindrical coordinates. Most of the variation is now seen to be contained within the radial in-plane normal strain component ϵ_{rr}. The sign of the change is consistent with the relaxation of compressive in-plane strain in the epilayer, while the ϵ_{zz} component (unchanged from the

Cartesian representation) shows the corresponding reduction in the *c* lattice parameter expected in the case of biaxial strain.

4. Discussion

To investigate the relaxation of the in-plane compressive strain in the vicinity of the mesa perimeter, we can plot the relevant element of the strain tensor at a given pixel against its corresponding radial coordinate *r*. When repeated for all pixels in the map, the resultant 2-dimensional histogram (lower graph in figure 6) shows the strain relaxing with increasing distance from the reference at the compressively strained mesa centre, before the strained underlying layer in the edged region beyond the mesa is again sampled. When plotted on a log scale (figure 7), this is seen to vary exponentially, with a characteristic relaxation length in this case of $L_{1/e} \approx 4\,\mu\text{m}$.

A similar correlation can be seen in the radial dependence of the CL peak energy for the AlGaN layer (upper plot in figure 6). The additional scatter in this plot reflects the inherent inhomogeneity in the CL of the wafer, present in both the mesa and etched regions.

To make a direct comparison between the EBSD-derived strain and its CL-determined effect, we plot histograms in figure 8 correlating these two parameters, again using the 4.7–4.8 eV AlGaN CL peak. For clarity, we have separated the regions within and outwith the mesa perimeter. These show a clear relationship between radial in-plane strain and emission energy in the mesa (lower plot), while the uniformly-strained etched region shows—as expected—no such effect (upper plot).

It is interesting to note the appearance of six-fold rotational symmetry in the $\epsilon_{\theta\theta}$ (i.e. azimuthal) strain component map (figure 5, centre). The effect is small, and is only visible after projection into the new coordinate system. While this strain component map reflects the symmetry of the wurtzite crystal structure, such an effect would *not* be an expected consequence of a simple relaxation of the in-plane compressive strain. The elastic constants of crystals with hexagonal symmetry are well known to be in-plane isotropic, meaning for example the components of Young's modulus in the *a* $\langle 11\bar{2}0 \rangle$ and *m* $\langle 10\bar{1}0 \rangle$ crystal directions should be identical. One reason for the observed symmetry could be the etching process, which, in a reversal of the effect seen in anisotropic growth rates [12], could result in a non-circular mesa and an anisotropic strain field; we see no evidence for this in the electron image of figure 1, though. It may instead be the case that the relaxation (and therefore expansion) of material around the mesa perimeter has resulted in a subtle 'buckling' of the epilayer, giving 6-fold periodically alternating regions of different azimuthal normal strain.

In order to aid visualization of the normal in-plane tensor elements ϵ_{rr} and $\epsilon_{\theta\theta}$, figure 9 shows exaggerated cartoons illustrating the effects of these two components on a uniform (r, θ) grid, varying in a manner similar to our observations. The top grid shows the unstrained case, while the left-hand grid shows the effect of the radial strain ϵ_{rr} increasing at the
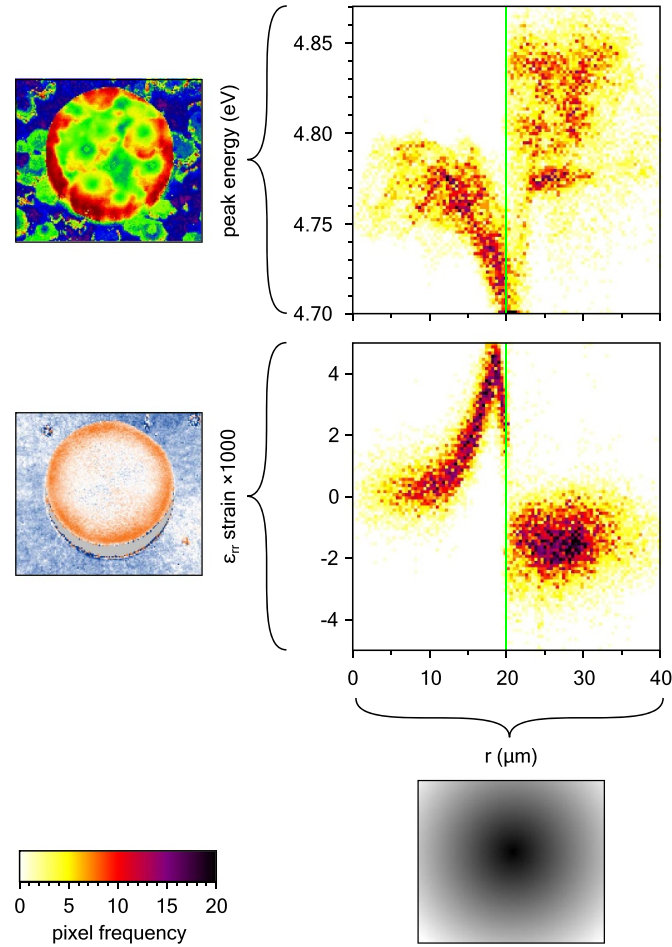
Figure 6. 2-dimensional histograms showing the radial distance (r) dependence of (upper) the AlGaN layer CL peak energy (from figure 3); and (lower) the ϵ_{rr} normal strain component (from figure 5). Green vertical lines mark the position of the mesa perimeter at $r = 20\,\mu$m.
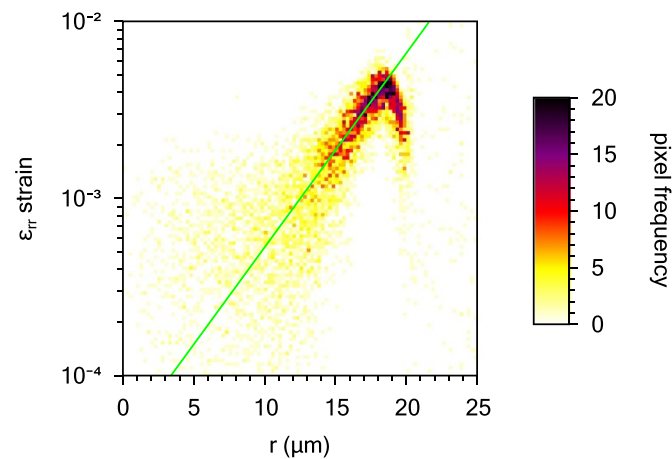

Figure 7. The r dependence of the ϵ_{rr} radial normal strain (from the lower plot in figure 6) on a semi-logarithmic scale. The guide line represents a characteristic relaxation length of $L_{1/e} = 4\,\mu$m.

mesa edge, and the right-hand grid shows the azimuthal $\epsilon_{\theta\theta}$ varying with 6-fold symmetry.

We can compare the orientation of the nodes of this azimuthal strain with the crystal directions of the epilayer. Figure 10 shows the upper-hemisphere stereoscopic-projection pole figures for the $\{0001\}$ and $\{10\bar{1}0\}$ directions,
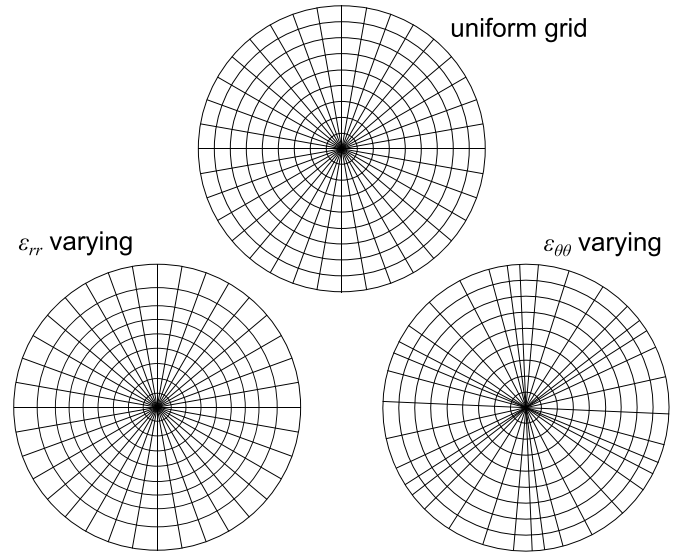
calculated from the same EBSD dataset using conventional Hough transform analysis. The spots indicate projections of the experimentally determined crystal direction, repeated for all pixels in the map. The central position of the $\{0001\}$ spot (left) shows the layer to be *c*-plane, as expected, while the orientation of the $\{10\bar{1}0\}$ spots (right) shows convincing
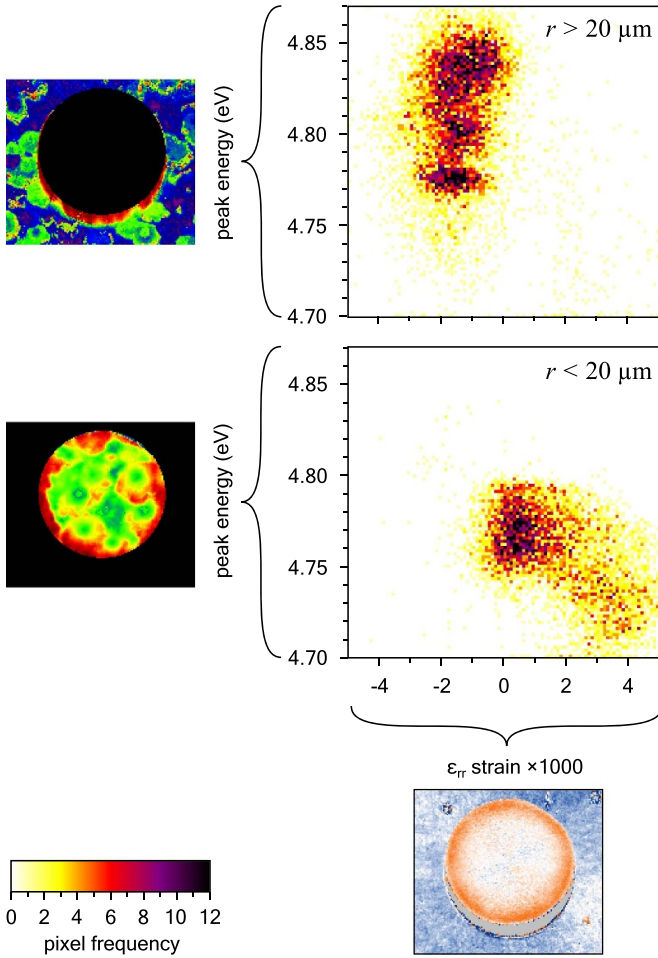
Figure 8. (Right) 2-dimensional histograms showing the pixel-wise correlation between the 4.7–4.8 eV CL peak energy and the ϵ_{rr} normal strain component. For clarity, these are split into regions outwith (upper) and within (lower) the 20 μm radius mesa.

Figure 9. Exaggerated cartoons separately showing the effects of the two in-plane normal strain components, with (top) the unstrained case, (left) ϵ_{rr} increasing towards the mesa edge, and (right) $\epsilon_{\theta\theta}$ varying with rotational periodicity.
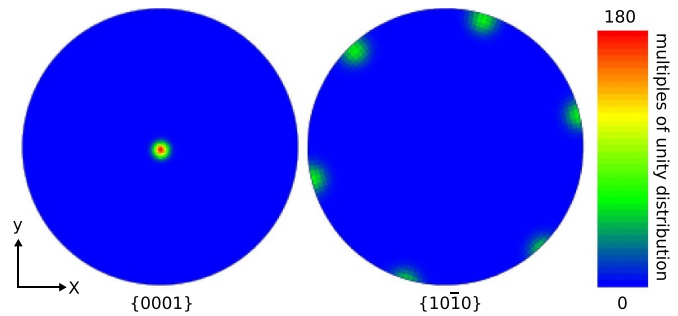
Figure 10. Upper hemisphere pole figures generated from the same EBSD dataset as the strain maps and displayed using a stereoscopic projection.

correspondence with that of the nodes seen in the $\epsilon_{\theta\theta}$ map (figure 5, centre). In other words, within the relatively relaxed near-perimeter region, the azimuthal normal strain component $\epsilon_{\theta\theta}$ shows maxima along the $\{10\bar{1}0\}$ *m* directions and therefore minima along the $\{11\bar{2}0\}$ *a* directions. Such orientation-dependent deformation has been observed in other crystal structures [13].

While this combination of techniques will be valuable for analysing back-emitting samples such as the one presented here, it will not be applicable to the more general case, where the light can often not be collected through the substrate. We also note some potential limitations. Firstly, the accelerating voltage required for the EBSD is higher than that normally chosen for CL, resulting in a luminescence excitation volume which is both wider and deeper than usual. The effect of this on the data will depend on the sample. Samples where the CL comes from a thin top layer will be largely unaffected, as the emission will come from a region where there has been limited beam spreading. For a bulk material, the effect will be a worsening of the spatial resolution. For some samples, the higher penetration depth may actually be desirable, as in this case when we are looking at the buried *n*-AlGaN layer. A

second consideration is that the regions from which the EBSD and CL signals originate are not entirely coincident, with the EBSD signal carrying information much more dependent on the strain state in the near-surface region.

5. Conclusions

In conclusion, we have exploited the transparent substrate of UVLEDs, an unconventional detector geometry, and high-resolution cross-correlation-based analysis to achieve simultaneous mapping of the elastic strain tensor and luminescence spectrum in a microLED. The results show that the relaxation of strain around the edges of a microLED mesa has a measurable effect on the emission wavelength of the device. While confirming previous results which used CL hyperspectral imaging alone, this combination of techniques has unambiguously correlated the observed effect with a direct measurement of the strain. This eliminates other potential causes for the shifts in emission wavelength, for example surface recombination effects or mesa-size-dependent variations in current density.

Furthermore, transformation of the strain tensor maps from a general coordinate system (Cartesian) into one more specifically adapted to the geometry of the device (cylindrical polar) has allowed us to draw out subtle and previously unnoticed variations in the strain maps which give further insight into the nature of the deformation which results from the relation of strain in such structures.

Data availability statement

The data that support the findings of this study are openly available at the following URL/DOI: https://doi.org/10.15129/62ff6ef5-c084-422f-b180-0b50b2927fe8 [14].

Acknowledgments

ORCID iDs

Paul R Edwards ⬤ https://orcid.org/0000-0001-7671-7698
G Naresh Kumar ⬤ https://orcid.org/0000-0002-9642-8137
Jonathan J D McKendry ⬤ https://orcid.org/0000-0002-6379-3955
Enyuan Xie ⬤ https://orcid.org/0000-0001-7776-8091
Erdan Gu ⬤ https://orcid.org/0000-0002-7607-9902
Martin D Dawson ⬤ https://orcid.org/0000-0002-6639-2989
Robert W Martin ⬤ https://orcid.org/0000-0002-6119-764X

References

[1] Bertram F, Riemann T, Christen J, Kaschner A, Hoffmann A, Thomsen C, Hiramatsu K, Shibata T and Sawaki N 1999 Strain relaxation and strong impurity incorporation in epitaxial laterally overgrown GaN: direct imaging of different growth domains by cathodoluminescence microscopy and micro-Raman spectroscopy *Appl. Phys. Lett.* **74** 359–61

[2] Xie E Y *et al* 2012 Strain relaxation in InGaN/GaN micro-pillars evidenced by high resolution cathodoluminescence hyperspectral imaging *J. Appl. Phys.* **112** 013107

[3] Piazolo S, Prior D J and Holness M D 2005 The use of combined cathodoluminescence and EBSD analysis: a case study investigating grain boundary migration mechanisms in quartz *J. Microsc.* **217** 152–61

[4] Hu Y, Kusch G, Adeleye D, Siebentritt S and Oliver R 2024 Characterisation of the interplay between microstructure and opto-electronic properties of Cu(In,Ga)S$_2$ solar cells by using correlative CL-EBSD measurements *Nanotechnology* **35** 295702

[5] Wilkinson A J, Meaden G and Dingley D J 2006 High-resolution elastic strain measurement from electron backscatter diffraction patterns: new levels of sensitivity *Ultramicroscopy* **106** 307–13

[6] Vilalta-Clemente A, Naresh-Kumar G, Nouf-Allehiani M, Gamarra P, di Forte-Poisson M A, Trager-Cowan C and Wilkinson A J 2017 Cross-correlation based high resolution electron backscatter diffraction and electron channelling contrast imaging for strain mapping and dislocation distributions in InAlN thin films *Acta Mater.* **125** 125–35

[7] Naresh-Kumar G *et al* 2022 Non-destructive imaging of residual strains in GaN and their effect on optical and electrical properties using correlative light-electron microscopy *J. Appl. Phys.* **131** 075303

[8] He X, Xie E, Islim M S, Purwita A A, McKendry J J D, Gu E, Haas H and Dawson M D 2019 1 Gbps free-space deep-ultraviolet communications based on III-nitride micro-LEDs emitting at 262 nm *Photon. Res.* **7** B41–B47

[9] Kneissl M, Seong T-Y, Han J and Amano H 2019 The emergence and prospects of deep-ultraviolet light-emitting diode technologies *Nat. Photon.* **13** 233–44

[10] Edwards P R, Jagadamma L K, Bruckbauer J, Liu C, Shields P, Allsopp D, Wang T and Martin R W 2012 High-resolution cathodoluminescence hyperspectral imaging of nitride nanostructures *Microsc. Microanal.* **18** 1212–9

[11] Bower A F 2009 *Applied Mechanics of Solids* 1st edn (CRC Press) (https://doi.org/10.1201/9781439802489)

[12] De Donno M, Albani M, Bergamaschini R and Montalenti F 2022 Phase-field modeling of the morphological evolution of ringlike structures during growth: thermodynamics, kinetics and template effects *Phys. Rev. Mater.* **6** 023401

[13] Das S, Yu H, Mizohata K, Tarleton E and Hofmann F 2020 Modified deformation behaviour of self-ion irradiated tungsten: a combined nano-indentation, HR-EBSD and crystal plasticity study *Int. J. Plast.* **135** 102817

[14] Edwards P, Gunasekar N and Martin R 2024 Simultaneously acquired maps of electron backscattered diffraction patterns and cathodoluminescence spectra from an ultraviolet micro-light-emitting diode *University of Strathclyde KnowledgeBase* (https://doi.org/10.15129/62ff6ef5-c084-422f-b180-0b50b2927fe8)